Available online at www.sciencedirect.com
SCIENCE DIRECT®
Journal of Solid State Chemistry 177 (2004) 281–292
JOURNAL OF SOLID STATE CHEMISTRY
http://elsevier.com/locate/jssc

Chemistry and thermodynamics of the twin charge-ordering transitions in $RBaFe_2O_{5+w}$ series

P. Karen*

Department of Chemistry, University of Oslo, P.O. Box 1033, Blindern N-0315 Oslo, Norway

Received 19 May 2003; received in revised form 25 July 2003; accepted 7 August 2003

Abstract

Thermal and volume parameters of the twin charge-ordering Verwey transitions in $RBaFe_2O_{5+w}$ (R = a rare-earth element) are summarized as a function of R and w. Their determination is exemplified for case R = Dy, for which also synthesis conditions, phase relations, and refined crystal-structure data for the valence-mixed ($Fe^{2.5+}$) and charge-ordered (Fe^{2+} and Fe^{3+}) phases are reported. Data for the R = Nd, Sm, Eu and Gd variants with wide ranges of oxygen non-stoichiometry suggest that increasing w decreases ΔS and the temperature of the transition in a manner that is similar to a behavior under increasing concentration of an ideal solution of $RBaFe_2O_6$ in $RBaFe_2O_5$. Thermal parameters of the transition for the ideal mixed-valence composition $RBaFe_2O_{5.000}$ are estimated from such compositional dependences, varying reasonably smoothly as a function of R (radius, electronegativity, polarizability). Parameter ΔV is the only one that follows the structural discontinuity between the charge-ordered R = Nd and variants with smaller trivalent R ions. The ordering of the d_{xz} orbitals of the Fe^{2+} ions is thus being achieved at a cost of lowering the symmetry when the R size becomes unfavorably large. A definition of the Verwey transition as a first-order orbital ordering of a valence-mixed phase is suggested.

Keywords: Mixed-valence classes; Verwey-transition thermodynamics; Depression of charge-freezing point by non-stoichiometry; Synchrotron X-ray diffraction; Charge-ordering superstructure; Rare-earth barium iron oxides

1. Introduction

There are thousands of compounds that fulfill one of the Day–Robin definitions [1] of the three classes of mixed valence. As noted by Mott [2], only a few of them change from one class to another as a function of temperature. To date there is only one structural type that makes the metamorphosis through all three Day–Robin classes, via two first-order phase transitions [3,4]. It is $RBaFe_2O_5$, a double-cell perovskite in which the small size of the trivalent rare-earth ion R^{3+} (R = Nd–Ho and Y) stabilizes an oxygen vacancy, and the divalence of the large barium ion introduces the charge imbalance that forces the semi-integer valence upon iron.

As a class-III mixed-valence paramagnetic conductor above $T_N \approx 430$ K, the phase has a tetragonal structure of the $P4/mmm$ symmetry. Below the Néel temperature, an increasing orthorhombic distortion appears ($Pmmm$), associated with alignment of the antiferromagnetic moments in a direction perpendicular to the tetragonal four-fold axis (viz., along b) [4]. Given the typical shape of the d_{xz} orbitals, the magnetostrictive contraction along b offers, together with the corresponding expansion along a, an opportunity for ordering of these orbitals [3], minimizing their energy and allowing them to be doubly occupied in case of a high-spin d^6 ion, such as Fe^{2+}. Mössbauer spectroscopy has shown [3] that at a certain temperature below T_N a premonition of the full charge ordering occurs within this minor orthorhombic distortion, when the single valence-mixed state $Fe^{2.5+}$ separates into two states $Fe^{2.5-\varepsilon}$ and $Fe^{2.5+\varepsilon}$, corresponding to the Day–Robin class-II mixed valence. This premonitory charge-ordering transition is manifested by a relatively small caloric effect and a small increase in electrical resistivity. No structural changes are detected by either synchrotron X-ray or neutron powder diffraction [4,5]. Upon further cooling, a full separation into integer charges of the class-I mixed valence occurs at a temperature T_V referring to the Verwey transition observed first [6] in magnetite. The ensuing ordering of

*Fax: +47-22-85-54-41.
E-mail address: pavel.karen@kjemi.uio.no.

0022-4596/$ - see front matter © 2003 Elsevier Inc. All rights reserved.
doi:10.1016/j.jssc.2003.08.011

di- and trivalent iron is accompanied by a huge increase in orthorhombic distortion that minimizes the energy of the doubly occupied d_{xz} orbitals of Fe^{2+}. The long-range charge-ordered structure below the transition temperature T_V thus features alternate chains of di- and trivalent iron running along b, instead of their alternating in all three dimensions, as dictated [7] for point charges. The localization of the ionic charges is manifested by a two-orders-of-magnitude increase in electrical resistivity, an increase in volume and a decrease in entropy causing a proportionally stronger caloric effect than that observed at the premonitory charge-ordering transition. The magnitudes of these changes, as well as the transition temperatures T_V are strongly influenced by the type of the R atom (R = Nd [8], Sm [8], Eu [9], Gd [10], Tb [3], Y [4] and Ho [5]) that seemingly have little to do with the charge-ordering process of the iron atoms. This is not uncommon. Also in iron molecular complexes, moieties that are not coordinated to iron exhibit influence over the stability of the charge-ordered state [11].

For obvious reasons, the transition parameters are also strongly influenced by any departure from the ideal ratio of the integer iron valences caused by oxygen non-stoichiometry [8,12] or aliovalent doping [13]. The oxygen non-stoichiometry is of the $RBaFe_2O_{5+w}$ type with $w>0$, and the additional oxygen is accommodated at the vacant perovskite site situated in the R layer. Accordingly, the achievable occupancy of this site varies with the size of the R atom: from $w=0.03$ for R = Ho up to some $\frac{3}{4}$ filling for the largest compatible R = Nd at ambient oxygen pressures. This gives a wide range for the control of the average oxidation state of iron, from 2.5 for $w=0$ to 3 for $w=0.5$, and higher up. The most important effect of the oxygen non-stoichiometry is the progressive decrease of the concentration of the valence-mixed $Fe^{2.5+}$ state as seen by Mössbauer spectrometry. This decrease has been described by a probability model of pairing of neighboring integer ionic charges [12].

In this paper, thermodynamic description of Verwey transitions in $RBaFe_2O_{5+w}$ is attempted experimentally in terms of variables of thermal (ΔH, ΔS, T_c) and structural (ΔV) origin, which are summarized and analyzed as a function of R and w. For R = Dy as an example, determination of these variables is reported in detail, together with synthesis, phase relation data, and crystal structure refinements of the charge-ordered superstructure.

2. Experimental

2.1. Syntheses and oxygen-content control

Amorphous precursor for synthesis of $DyBaFe_2O_{5+w}$ was obtained from standardized Dy_2O_3 (99.9%, Stanford Materials), metallic iron (99.95%, Koch–Light) and barium carbonate (0.1% Sr, Merck) by liquid mixing in a citrate melt. The procedure is described in detail in Ref. [8]. Calcination was performed at 860°C in an atmosphere of Ar, H_2 and H_2O having $\log(p_{O_2}/\text{bar}) \approx -16$; yielding a single-phase powder. The master sample material was sintered in the form of cylinders (cold pressed at 150 kg/cm^2) at 1000°C under $\log(p_{O_2}/\text{bar}) \approx -15.2$. The oxygen non-stoichiometry (w) was controlled by high-temperature equilibration and quenching in similar atmospheres with partial pressures of oxygen defined by the humidity of the gas (measured by an Endress–Hauser MMY150 hygrometer). The equilibrated samples were quenched into a metal container filled with high-purity Ar (<2 ppm O_2, dried over a P_2O_5 desiccant). A thin surface layer was removed before further characterizations, and samples were stored under argon. The oxygen content was determined by a cerimetric method described in detail in Ref. [14]. The standard deviations of the titration may be judged from data presented in Section 3.1. For a typical distribution of the oxygen content across such quenched samples; see Ref. [10].

In an attempt to further improve the oxygen-content homogeneity, a sintered cylinder of $DyBaFe_2O_{5.006}$ was sealed in an evacuated quartz tube, annealed for 3 months at 250°C and gradually cooled down to ambient temperature over a 1-month period. The comparison of the thus obtained sample (new oxygen-content parameter $w=0.013$) with a sample that has not been annealed ($w=-0.004$) is in Section 3.4.

2.2. Phase-content determinations

All samples were characterized by conventional X-ray powder diffraction (XPD) with Guinier–Hägg camera, Cu$K\alpha_1$ radiation, using Si as an internal standard. Contents of crystalline phases were estimated from comparisons of calculated and observed intensities of prominent Bragg peaks fitted as Lorentzian profiles. All phase contents are listed in molar fractions x that refer to formula units where non-oxygen atoms are normalized to unity. This corresponds to expressing the composition in terms of coordinates in the subsolidus Dy(O)–Ba(O)–Fe(O) phase diagram.

2.3. Synchrotron powder X-ray diffraction (SXPD)

Data on $DyBaFe_2O_{5+w}$ were collected at the powder diffractometer with He cryostat installed on the BM1B beamline at the ESRF Grenoble in following sequences: (1) High-resolution, high-counting-statistics data collection for Rietveld refinement in the GSAS programme suite [15] of the long-range charge-ordered superstructure of the class-I mixed-valence phase at 100 or 200 K. (2) Isothermal scans upon warming through the Verwey transition over the 020-type Bragg peaks; for unit-cell

data from Lorentzian profile fits. (3) High-resolution data for Rietveld refinement of the class-III mixed-valence phase at 330 K. Data for Rietveld refinements were binned from all six Si-crystal analyzers of the diffracted beam currently installed at the diffractometer. For short scans only that analyzer was used whose angular position is directly calibrated. Samples were sealed in glass capillaries of 0.25 mm in diameter (calculated absorption $\mu R < 1$), spinning in the monochromatic X-ray beam of a cross-section of 1×5 mm^2 and wavelength $\lambda \approx 0.5$ Å calibrated with a NIST standard silicon. According to Ref. [10], the Bragg-line asymmetry observed for these phases arises from convolutions of the nearly Lorentzian instrumental profile with compositional distributions of unit-cell parameters. As such, it was modeled by releasing the linear strain coefficients S_{hkl} of Stephens [16] in the profile function based on the pseudo-Voigt function of Thompson et al. [17]. Although not all nuances of the unit-cell-parameter distributions can be contoured in this manner, the important peak/background resolution of the extremely weak superstructure peaks at the foothills of the strong peaks is good.

2.4. Differential scanning calorimetry (DSC)

A liquid-nitrogen operated Perkin–Elmer Pyris 1 instrument was used to monitor thermal-flux curves upon heating (10 K/min) between 160 and 360 K. Aluminum pans (50 μL) were used to seal the coarsely powdered samples. Temperatures were corrected to the zero sample-weight based on a peak-temperature dependence measured in a separate calibration series (the correction was rarely larger than 1 K). The temperature scale was calibrated on cyclopentane, cyclohexane, *n*-octane, *n*-decane, *n*-dodecane, *m*-nitrotoluene and *p*-nitrotoluene standards of >99.7% purity and found linear. Enthalpy was standardized on melting of the Perkin–Elmer standard indium as well as on the low-temperature phase transitions of cyclohexane. Standard deviations of these runs were typically ±1% of the value. Both the transition enthalpy and entropy were determined by integration of the heat-flow peaks, as described in Ref. [10].

3. Results and discussion

3.1. Formation of RBaFe$_2$O$_{5+w}$

In order to obtain a comprehensive picture of the redox stability of RBaFe$_2$O$_{5+w}$, a series of oxygen-control equilibrations has been performed at 1000°C on all R variants. In Fig. 1, partial pressures of oxygen that limit the formation of RBaFe$_2$O$_{5+w}$ are plotted as a function of R, including R = La, which forms a single-perovskite-type structure, and R = Er, which does not form a perovskite. It is seen that changing R varies dramatically the homogeneity limits of RBaFe$_2$O$_{5+w}$:

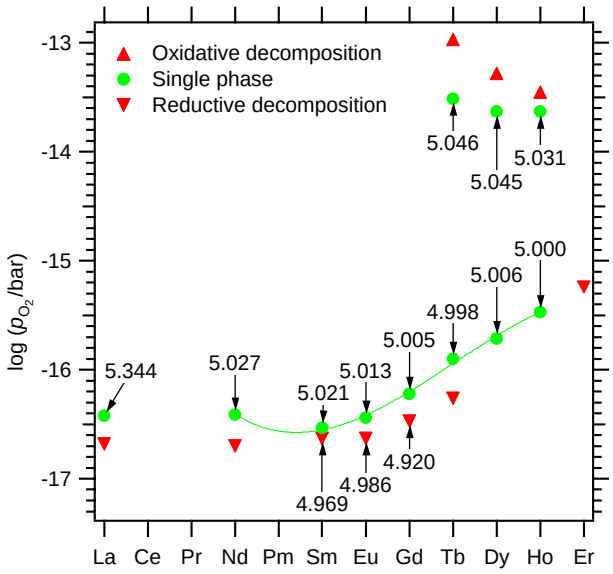

Fig. 1. Limits in partial pressures of oxygen for formation of RBaFe$_2$O$_{5+w}$ at 1000°C, as seen after 4 days of equilibration. Oxygen content per the nominal formula unit is listed for samples with majority phase RBaFe$_2$O$_{5+w}$.

Table 1
Decomposition products[a] upon oxidation of DyBaFe$_2$O$_{5+w}$ at 1000°C. Parameters estimated by molar balance are in italics

Oxygen content	DyFeO$_3$	Ba$_{1-y}$Dy$_y$FeO$_{3-w'}$			
	x	x	y	w'	a/Å
5.306(1)	0.21	0.79	*0.37*	*0.44*	3.9210(7)
5.424(4)	0.22	0.78	*0.36*	*0.37*	3.9211(5)

[a] For definition of the phase content x see Section 2.2.

Oxidation in pure oxygen of phases with R down to Gd does not cross the upper homogeneity limit at 1000°C. The stability window narrows substantially for variants with smaller R, as these phases become stable only in reducing atmospheres. Their oxidation upon gradually increasing partial pressure of oxygen proceeds sharply into multiphase products exemplified in Table 1 for R = Dy.

Reductive decomposition as a function of decreasing partial pressure of oxygen proceeds at 1000°C over an intermediate pseudo-equilibrium range into a dark-green product where iron has oxidation state close to +2 (by cerimetry; the phase identity was not ascertained). By correcting the redox conditions, the green product can be oxidized back to a single-phase double-cell perovskite. The intermediate range (Fig. 1) is approximately 0.2 bar wide in terms of oxygen partial pressure; about twice the estimated effect of the

Table 2
Syntheses and characterizations of nominal $DyBaFe_2O_{5+w}$ samples

Oxygen	Double-cell perovskite, XPD					log(p/bar)			
content[a]	x	a/Å	b/Å	c/Å	Ar : H_2[b]	H_2O	O_2	t/°C	τ/days
Not det.	0.31	3.9464(11)	3.9186(11)	7.5647(20)	8.78	−4.35	−28.54(1)	660	6
4.732(1)	0.57	3.9437(4)	3.9187(4)	7.5664(7)	8.78	−4.35	−28.84(1)	650	6
4.888(4)	0.65	3.9442(8)	3.9175(6)	7.5660(16)	8.78	−4.35	−29.15(1)	640	6
4.988(2)	1	3.9426(7)	3.9180(7)	7.5654(13)	8.78	−4.35	−29.46(1)	630	6
4.996(1)	0.992[c]	3.9440(5)	3.9181(5)	7.5626(10)	9.19	−3.99	−29.36(1)	610	5
5.006(1)	1	3.9440(4)	3.9175(3)	7.5639(9)	8.52	−1.62	−15.71(2)	1000	4
5.008(1)	1	3.9438(8)	3.9185(8)	7.5668(14)	8.78	−4.35	−29.78(1)	620	5
5.020(1)	1	3.9441(5)	3.9177(4)	7.5644(10)	18.2(1)	−1.65	−15.17(3)	1000	4
5.030(1)	1	3.9442(4)	3.9186(3)	7.5665(9)	82(2)	−1.76	−14.11(3)	1000	3
5.045(3)	1	3.9426(5)	3.9192(4)	7.5717(11)	123(3)	−1.70	−13.63(3)	1000	3
5.306(1)	0	—	—	—	198(6)	−1.74	−13.28(4)	1000	3
5.424(4)	0	—	—	—	332(18)	−1.70	−12.75(6)	1000	3

[a] Overall cerimetric oxygen content per nominal formula $DyBaFe_2O_{5+w}$.
[b] By volume; standard error refers to variations over time.
[c] According to SXPD; see Section 2.2 for definition of x.

variations in the composition of the flowing gas and the temperature of the wetting solution.

According to Fig. 1, single-phase $RBaFe_2O_{5+w}$ is formed over a w range that is narrowing towards smaller R ions and approaching simultaneously the ideal mixed-valence composition $w = 0.000$. In the particular case of $DyBaFe_2O_{5+w}$, single-phase compositions down to $w = 0.006$ are obtained at 1000°C (Table 2). However small, such compositional nuances are important for the three-dimensional long-range charge ordering to be detectable, the detection limit being $w \approx 0.02$ [8].

The ideal mixed-valence composition $DyBaFe_2O_{5.000}$ appears better achievable when the oxygen-content control procedure is performed at temperatures below 700°C. Decomposition under increasingly reducing conditions then proceeds with no apparent discontinuity in the overall (cerimetric) oxygen contents; as though the range of sluggish kinetics observed at 1000°C were much broader. Indeed, decomposition products gradually and clearly emerge and prevail as a function of increasing temperature when the reaction atmosphere and time are kept constant. While the overall oxygen contents of such mixtures decrease, unit-cell parameters of the original phase (Table 2) and of the decomposition products (Table 3) do not change. This is not compatible with thermodynamic equilibrium among these phases. The implied kinetic limitation was verified by investigating the deoxidation process isothermally at 650°C as a function of time (Table 3), in which the extent of decomposition increased steadily with time. Table 3 further lists concentrations of the decomposition products, which are metallic Fe, Dy_2O_3 and a cubic perovskite-type phase. Identification of the latter phase was attempted from Dy(O)–Ba(O)–Fe(O) phase-diagram considerations that dictate a composition with somewhat higher molar fraction of Ba than of Dy.

Table 3
Kinetic limitation of reductive decomposition of $DyBaFe_2O_{5+w}$ samples[a]

Oxygen	$\tau \approx 6$ days	$DyBaFe_2O_5$	$Ba(Dy,C)O_3$		Dy_2O_3	Fe
content	t/°C	x	x	a/Å	x	x
4.888(4)	640	0.65	0.07	4.216	0.04	0.24
4.732(1)	650	0.57	0.11	4.214	0.04	0.28
Not det.	660	0.31	0.22	4.209	0.07	0.40
	τ/days ($t = 650$°C)					
4.732(1)	6	0.57	0.11	4.214	0.04	0.28
Not det.	12	0.25	0.24	4.216	0.08	0.43
Not det.	18	0.13	0.27	4.212	0.11	0.49
Not det.	24	0.00	0.31	4.212(1)	0.12	0.57

[a] For other details on these samples see first three lines of Table 2. See also Section 2.2 for definition of x.

Intensities of the observed 110, 200, 211 Bragg reflections matched reasonably well with a solid-solution phase of composition related to $Ba_3Y_2CO_8$ [18,19]. The conjecture is that the triple-perovskite superstructure of the oxide-carbonate phase is not developed at these relatively low temperatures and only the disordered cubic-perovskite diffraction pattern is seen.

3.2. *Structure of the valence-mixed* $DyBaFe_2O_5$

SXPD data were collected at 330 K on $DyBaFe_2O_{5.013}$; the sample that had been annealed for several months in order to standardize the oxygen-content distribution (see Section 2). Small amounts of two other phases were identified: Fe [$x = 0.0069$, cubic, $a = 2.8687(16)$ Å] and Dy_2O_3 [$x = 0.0014$, cubic, $a = 10.6532(22)$ Å]. The refined pattern is shown in Fig. 2. For both impurity phases, only one strongest

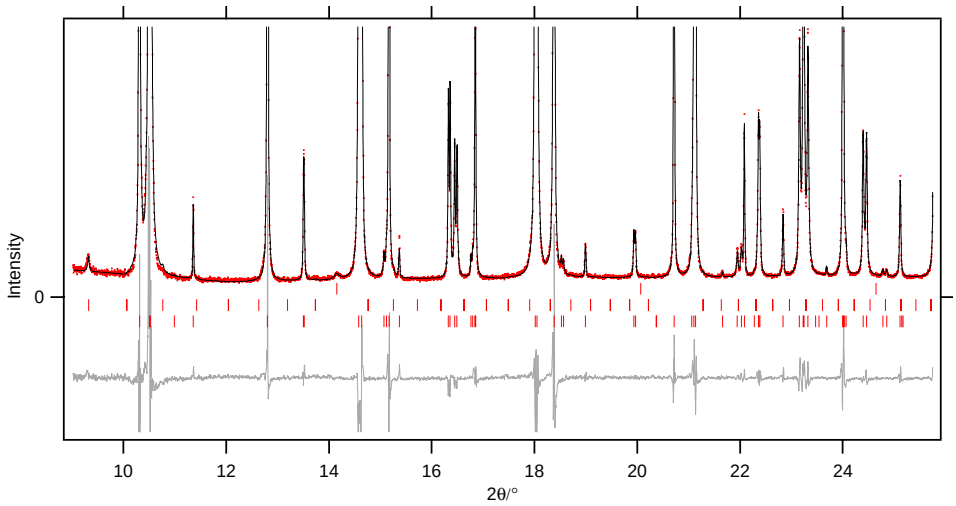

Fig. 2. Detail of the refined pattern ($\frac{1}{2}$ of angular and $\frac{1}{20}$ of intensity ranges) for $DyBaFe_2O_{5.013}$ at 330 K. The vertical bars denote Bragg reflections ($\lambda = 0.49981$ Å) for Fe (top), Dy_2O_3 (middle) and the *Pmmm* $DyBaFe_2O_{5.013}$ (bottom).

Table 4
Valence-mixed $DyBaFe_2O_5$ at 330 K; refined structure data

Unit-cell parameters		Refinement statistics	
Space group	*Pmmm*	R_{wp}	0.0562
a/Å	3.93855(1)	R_p	0.0443
b/Å	3.92433(1)	$R(F^2)$	0.0275
c/Å	7.57344(1)	N_{obs}	644
V/Å^3	117.056(0)	N_{vars}	33

Atom	Site	n	x	y	z	$100U_{iso}$
Dy	1*c*	1	0	0	1/2	0.52(1)
Ba	1*a*	1	0	0	0	0.52(1)
Fe	2*t*	1	1/2	1/2	0.2652(1)	0.51(1)
Fe′	2*t*	1	1/2	1/2	0.25	0.51(1)
O(1)	1*f*	1	1/2	1/2	0	0.92(4)
O(2)	2*s*	1	1/2	0	0.3101(3)	0.92(4)
O(3)	2*r*	1	0	1/2	0.3101(3)	0.92(4)
O(4)	2*r*	0.013	1/2	1/2	1/2	0.92(4)

Constraints: U_{iso}: Dy ≡ Ba, Fe ≡ Fe′, O(i) ≡ O(j); z: O(2) ≡ O(3), Fe′ fixed.

Bragg peak is identifiable in the diffraction pattern. Also other cubic sesquioxide formers, R = Ho and Y, yield the same phase composition under analogous synthesis conditions. The cerimetrically determined content of the added oxygens, $w = 0.013$, is taken under consideration in the Rietveld refinements by introducing a split site for iron, Fe′, corresponding to the fraction of irons that are in contact with the added oxygens. These Fe′ atoms have the z coordinate fixed to 0.25, which is believed to conform better with the local octahedral coordination. The refined data for the main phase are listed in Table 4.

3.3. *Structure of the charge-ordered* $DyBaFe_2O_5$

Two sets of SXPD data were collected at two different occasions, viz., a pattern at 200 K of the directly quenched $DyBaFe_2O_{4.996}$, and a pattern at 100 K of the long-term annealed $DyBaFe_2O_{5.013}$. The results of the Rietveld refinements of the charge-ordered superstructure in these two samples are combined in Table 5.

Table 5
Charge-ordered $DyBaFe_2O_{5.013}$ at 100 K and $DyBaFe_2O_{4.996}$ at 200 K (in italics); refined structure data

Unit-cell parameters		Refinement statistics	
Space group	*Pmma*	R_{wp}	0.0900
			0.0849
a/Å	8.03833(4)	R_p	0.0692
	8.04527(3)		*0.0613*
b/Å	3.84648(2)	$R(F^2)$	0.0307
	3.85127(1)		*0.0231*
c/Å	7.54026(4)	N_{obs}	784
	7.54680(3)		*584*
V/Å^3	233.139(2)	N_{vars}	38
	233.834(1)		*36*

Atom	Site	n	x	y	z	$100U_{iso}$
Dy	2*c*	1	0	0	1/2	0.19(2)
						0.33(4)
Ba	2*a*	1	0	0	0	0.16(3)
						0.34(4)
Fe(1)	2*f*	1	1/4	1/2	0.2547(7)	0.23(2)
					0.2545(9)	*0.26(4)*
Fe(2)	2*f*	1	3/4	1/2	0.2683(6)	0.23(2)
					0.2692(7)	*0.26(4)*
O(1)	2*f*	1	1/4	1/2	−0.001(5)	0.12(8)
					0.002(7)	*0.40(12)*
O(2a)	2*e*	1	3/4	0	0.318(4)	0.12(8)
					0.314(6)	*0.40(12)*
O(2b)	2*e*	1	1/4	0	0.308(4)	0.12(8)
					0.314(6)	*0.40(12)*
O(3)	4*j*	1	0.0152(13)	1/2	0.3098(6)	0.12(8)
			0.0149(9)		*0.3114(7)*	*0.40(12)*
O(4)	2*f*	0.013	1/4	1/2	1/2	0.12(8)

Constraints: U_{iso}: Fe(1) ≡ Fe(2), O(i) ≡ O(j); $n_{O(4)}$ fixed.

The refinement itself is not straightforward because the Bragg superstructure intensities are extremely weak. Several such peaks are marked in a detail of the refined pattern shown in Fig. 3 (see Ref. [10] for a typical full pattern). None of them coincides with any calculated Bragg line of the two impurity phases. Only one impurity Bragg reflection (the strongest of Dy_2O_3) is identifiable in these low-temperature patterns. This is because the Fe 1 1 0 Bragg peak seen in the high-temperature pattern is hidden in one of the strong peaks of the main phase (cf. Fig. 2).

As established in Ref. [10], a distribution of the oxygen contents in the sample is responsible for the specific asymmetry of the Bragg peaks in these phases. In Ref. [10] such a distribution is estimated for $GdBaFe_2O_{5+\bar{w}}$ via. deconvolution of suitable Bragg-peak profiles with the instrument-width profile according to dependence of the unit-cell parameters on w. This approach is not fully applicable in the present case, because unit-cell parameters cannot be established over a sufficiently wide range of w. Nevertheless, peak profiles for $R = $ Gd and Dy show both the same type and magnitude of the asymmetrical peak broadening: The Bragg-profile tailing in Figs. 2 and 3 is of the same orientation in both the charge-ordered and valence-mixed states, and this correlates with the orthorhombic distortion diminishing and c increasing as a function of w. The asymmetry is best observed for the 4 0 0, 0 2 0, 0 0 4 Bragg peaks, which are situated between 13.5 and 15° 2θ (Fig. 3). Because the orthorhombic distortion for the low-temperature charge-ordered phase is much larger than for the high-temperature valence-mixed phase, the asymmetry effect is enhanced, in particular between the orthorhombically split peaks of the $h00$ and $0\frac{h}{2}0$ type, whose asymmetry is directed against each other forming a locally enhanced background. A pseudo-multiphase model was used in Ref. [10] for refinements of this type of enhanced background. Given that none of important superstructure Bragg intensities is directly affected by this feature, the pseudo-multiphase refinement was not used in the present study because it has the undesirable effect of causing refinement instabilities and creating false minima. However, two of six superstructure-related coordinates proved somewhat unstable, viz., the z coordinates of O(2a) and O(2b) that also differ most between the two cases of the charge-ordered superstructure refinement reported here. Assuming that random variations in the collected pattern are likely to affect the extremely weak superstructure intensities, taking an average of atomic coordinates from these two refinements appears as the best solution to arrive at values representative of the charge-ordered structure.

The averaged atomic coordinates from Table 5 were used to calculate bond distances and bond valence sums (BVS) for $DyBaFe_2O_5$ within the 200 K unit-cell dimensions (Table 6). Single-bond lengths by Brown [20] are used for metal ions, of which Fe^{2+} is located at the Fe(2) site and Fe^{3+} at the Fe(1) site, by comparison of bond distances. It is seen that these distances are close to those obtained by neutron powder diffraction for the $R = $ Tb [3], Y [4] and Ho [5] version, but differ from data obtained for $R = $ Gd [10] that are based on a single SXPD pattern collected with a less good statistics and refined with the pseudo-multiphase model. Somewhat surprisingly, the bond-distance errors cancel when BVS are calculated, and also BVS for $R = $ Gd are consistent with data for the other R variants, as shown in Fig. 4 for the case of iron atoms.

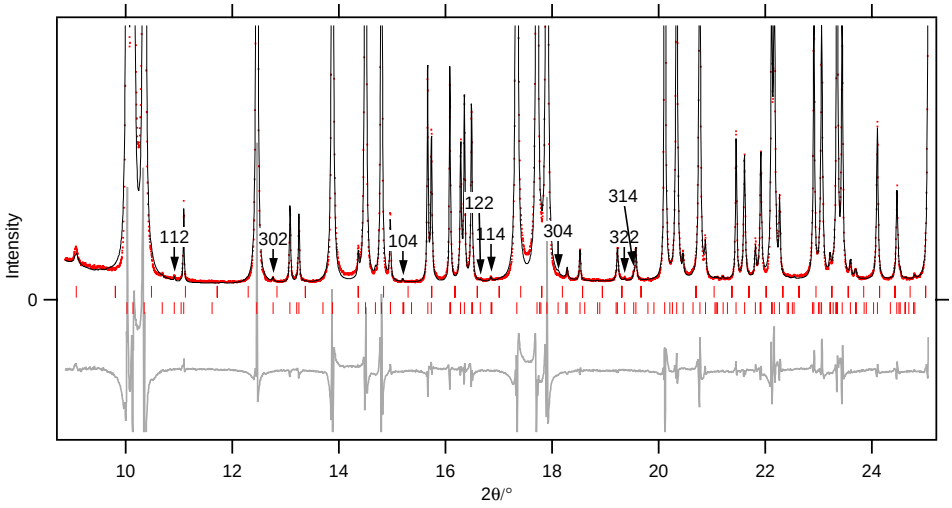

Fig. 3. Detail of the refined pattern (0.616 of angular and $\frac{1}{20}$ of intensity ranges) for class-I (charge-ordered) $DyBaFe_2O_{4.996}$ at 200 K. The vertical bars denote Bragg reflections ($\lambda = 0.48572$ Å) for Dy_2O_3 (top) and the *Pmma* $DyBaFe_2O_{5.013}$ (bottom). Superstructure Bragg reflections are marked with their *hkl* values where visually resolved on this scale.

Table 6
Bond distances (in Å) and bond valence sums (BVS) for charge-ordered $DyBaFe_2O_5$ at 200 K

Atom	Dy	Ba	Fe(1)	Fe(2)	Oxygen BVS
O(1)		4 × 2.7845(1)	1 × 1.921(60)	1 × 2.029(58)	2.13(17)
O(2a)	2 × 2.444(26)	2 × 3.120(35)		2 × 1.958(9)	1.96(9)
O(2b)	2 × 2.466(26)	2 × 3.091(34)	2 × 1.972(11)		1.98(10)
O(3)	4 × 2.401(3)	4 × 3.036(4)	2 × 1.937(5)	2 × 2.155(9)	1.95(3)
Metal BVS	2.78(10)	2.00(5)	3.00(16)	2.18(11)	

Averaged atomic coordinates from Table 5 are used, see also Supporting information. O(4) (≡ *w*) is neglected.

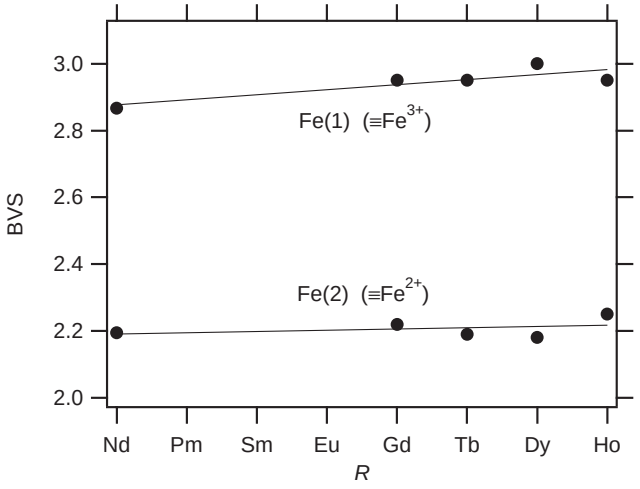

Fig. 4. Bond-valence sums for the two crystallographically different iron atoms calculated from structure data [3,5,10] for charge-ordered $RBaFe_2O_5$ at various low temperatures.

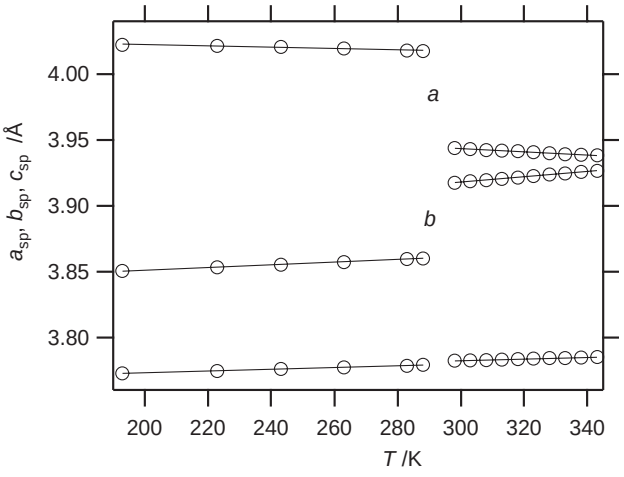

Fig. 5. Evolution of the SXPD-based dimensions per a single-perovskite-type cell across the Verwey transition in $DyBaFe_2O_{4.996}$ upon warming.

3.4. Characteristics of the Verwey transition in $DyBaFe_2O_5$

Evolution of the unit-cell parameters, volume, phase contents, and of the thermal effect upon warming through the mixed-valence class I–II transition and class II–III transition is illustrated on the example of *R* = Dy. The unit-cell data for $DyBaFe_2O_{4.996}$ (quenched) in Fig. 5 reveal a discontinuous change at the main Verwey transition (class I–II) whereas no discontinuity at the weak class II–III transition.

The gradual increase in the content of the valence-mixed phase, appearing at the expense of the charge-ordered phase upon warming through the main Verwey transition, is illustrated in Fig. 6 for the $DyBaFe_2O_{5.013}$ (annealed) sample. The appropriate DSC heat-flow peak is drawn for comparison. When differentiated, the formation of the valence-mixed phase contours the shape of the DSC peak, confirming that the oxygen-content distribution in the sample contributes to the DSC peak width. Determination of the volume change is illustrated in Fig. 7 for $DyBaFe_2O_{4.996}$. Note the lack of any observed volume change at the weak class II–III transition. Transition temperatures and thermal parameters are listed in comparison with other *R* variants in Section 3.6.

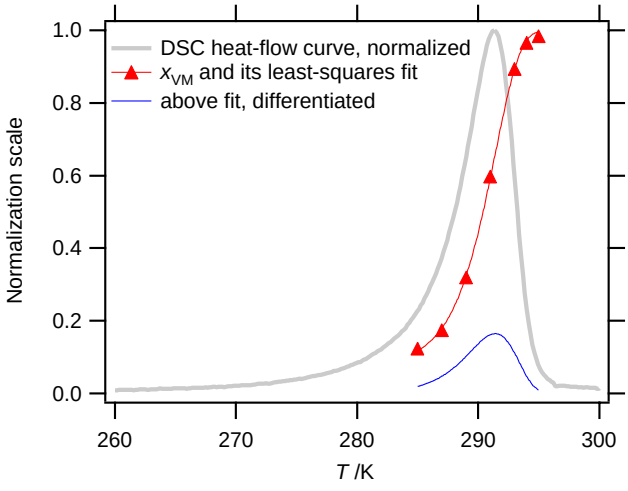

Fig. 6. Mole fraction x_{VM} of the valence-mixed phase $DyBaFe_2O_{5.013}$ upon warming through the main Verwey transition; according to SXPD. DSC trace drawn for comparison.

DSC traces in Figs. 6 and 7 refer the two different samples that were quenched at first, but one of them was

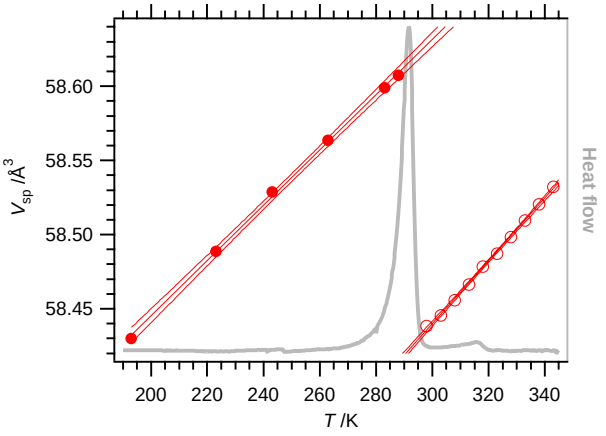

Fig. 7. Determination of the volume per single-perovskite-type cell of $DyBaFe_2O_{4.996}$ upon warming through the main Verwey transition; according to SXPD. DSC trace is used to localize T_V.

subsequently thermally equilibrated and then slowly cooled in a closed system (at 250°C, see Section 2 for details). Comparison of the DSC traces shows that both have practically identical shape. When the sigmoid curves for the evolution of the valence-mixed phase, such as that shown in Fig. 6, are compared in a similar manner, a slightly broader temperature range is seen for the equilibrated sample than for the sample that was only quenched. Together with the same pattern of Bragg-peak broadening for these two samples, this suggests that no improvement in sharpness of the oxygen-content distribution across the bulk is achieved during a subsequent thermal equilibration of once quenched sample.

3.5. *Oxygen non-stoichiometry and thermodynamics of Verwey transition in* $R\mathrm{BaFe_2O_{5+w}}$

As noted in Section 1, ^{57}Fe Mössbauer spectroscopy has been used [12] to account for the valence-mixed and charge-ordered states of iron in $R\mathrm{BaFe_2O_{5+w}}$, regardless of the disorder caused by the added oxygen w and whether or not their transition is discontinuous. Despite the progressive decay of these states with increasing w, traces of the valence-mixed state are still detected at non-stoichiometry levels as high as $w = 0.35$ [12]. However, as manifested by DSC on the enthalpy change and by diffraction methods on the volume change, the electron localization is discontinuous only to some $\frac{2}{3}$ of such a range. Along this interval in w, the changes in enthalpy, entropy, and volume across the main Verwey (class I–II) transition become zero, from a maximum seen at $w = 0$.

In line with the analogy between charge ordering and freezing of water, Ref. [10] considered the Verwey transition enthalpy of non-stoichiometric $R\mathrm{BaFe_2O_{5+w}}$ being analogous to the latent heat of a freezing/thawing solution. When $R\mathrm{BaFe_2O_5}$ is taken as the solvent and $R\mathrm{BaFe_2O_6}$ as the solute (the solute concentration is w), the transition temperature T_V decreases as a function of w in the manner that is consistent with the freezing-point depression by the thus defined solute. Assuming zero solubility in the solid solvent, the equality of chemical potentials for the pure solvent in both phases yields a simple expression for the composition dependence of T_V when the latent heat of fusion of the pure solvent is considered independent of temperature:

$$T_V(w) = \frac{\Delta H(0)}{\Delta S(0) - R\ln(1-w)}. \quad (1)$$

The parameters $\Delta H(0)$ and $\Delta S(0)$ refer to the pure solvent ($w = 0$). The analogy with the latent heat suggests that the transition enthalpy should decrease linearly with increasing concentration of the solute,

$$\Delta H(w) = \Delta H(0)\left[1 - \frac{w}{w(0)}\right] \quad (2)$$

as it can be imagined that each added oxygen atom takes away several unit cells from the pool of the valence-mixed/charge-ordered states, decreasing thus the amount of the solution that freezes discontinuously. Given that

$$T_V(w) = \frac{\Delta H(w)}{\Delta S(w)}, \quad (3)$$

the composition dependence of the transition entropy, $\Delta S(w)$, is expressed by substitution of $T_V(w)$ in Eq. (1) from Eqs. (3) and (2) and used together with Eq. (2) to fit simultaneously, by least squares, the experimental composition dependences $\Delta S(w)$ and $\Delta H(w)$. The three free parameters of such fits were chosen to be the fusion enthalpy and entropy of the pure 'solvent', $\Delta H(0)$ and $\Delta S(0)$, and the non-stoichiometry $w(0)$ where the former two values become zero.

The fits of the above model to the experimental thermal data of the main Verwey transition in $R\mathrm{BaFe_2O_{5+w}}$ are shown in Fig. 8. For phases with wide ranges of oxygen non-stoichiometry (R = Nd [8], Sm [8], Eu [9] and Gd [10]), all three parameters are refined (Table 7), for the other phases (R = Tb [3], Dy, Y [4] and Ho [5]) the parameter $w(0)$ has been fixed to 0.25. The reason for this is apparent from Fig. 8 where the $w(0)$ values vary only moderately for R = Sm, Eu and Gd, and the increases in $\Delta H(0)$ are compensated by the slope of $\Delta H(w)$ being steeper. Notably, R = Nd deviates from the other variants by having $\Delta H(0)$, $\Delta S(0)$, and $w(0)$ distinctly smaller. This discontinuity correlates with the change in symmetry of the charge-ordered structure, from *Pmma* to $P2_1ma$ for $NdBaFe_2O_5$ [5,8]. The $w(0)$ values, being close to $\frac{1}{4}$, may imply that one added oxygen atom takes away four unit cells (formula units) from the long-range charge (and orbital) order. This appears reasonable, considering that one oxygen

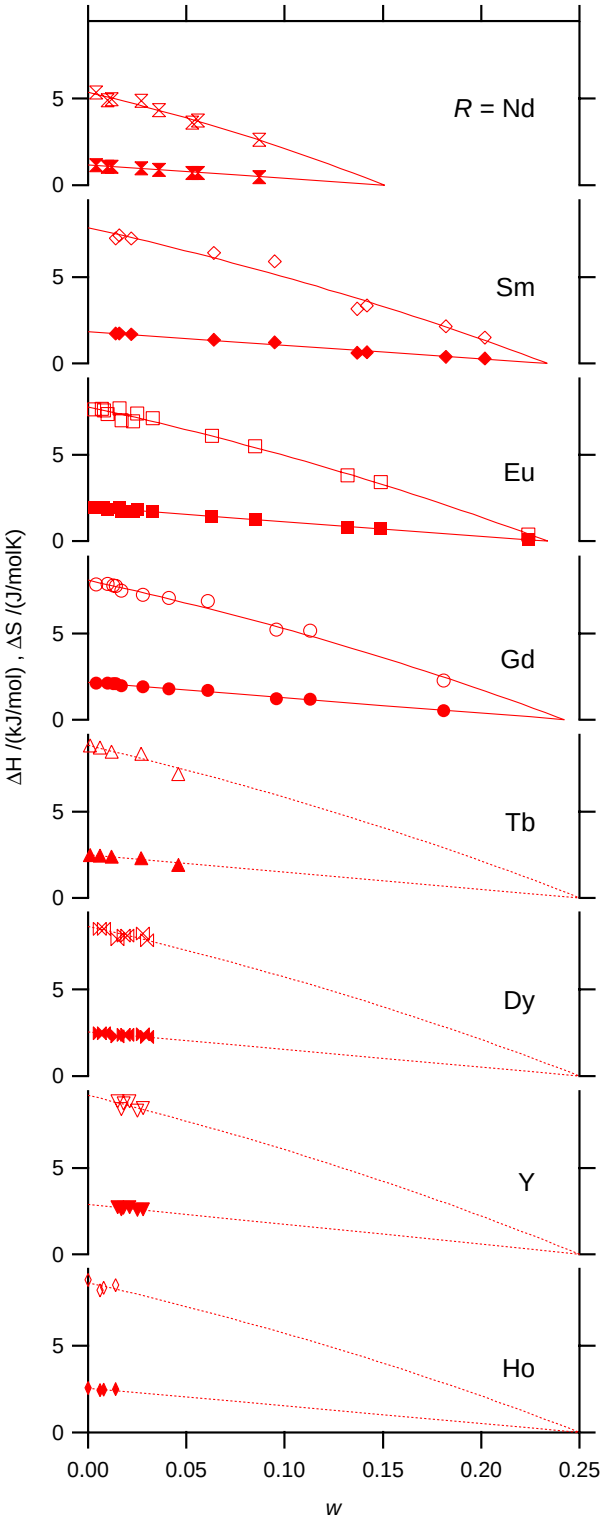

Fig. 8. Experimental $\Delta S(w)$ and $\Delta H(w)$ data for the main Verwey transition in $R\mathrm{BaFe_2O_{5+w}}$ and their fits according to the model for depression of the freezing point (see text for details).

atom oxidizes two divalent iron atoms into trivalent, and assuming that the unit cells facing these newly oxidized trivalent irons across the R structural layer may not be able to participate in the valence mixing and

Table 7
Fit parameters of the depression of freezing point model for $R\mathrm{BaFe_2O_{5+w}}$ to the experimental $\Delta S(w)$ and $\Delta H(w)$ data points for the main Verwey transition (Fig. 8)

R	$\Delta H(0)$	$\Delta S(0)$	$w(0)$	$-\Delta H(0)/w(0)$
	kJ/mol	J/(mol K)		kJ/mol
Nd	1.14(5)	5.38(7)	0.151(4)	−7.54(45)
Sm	1.83(14)	7.86(16)	0.234(5)	−7.84(66)
Eu	1.98(4)	7.79(5)	0.234(3)	−8.48(22)
Gd	2.16(6)	8.08(6)	0.242(4)	−8.92(29)

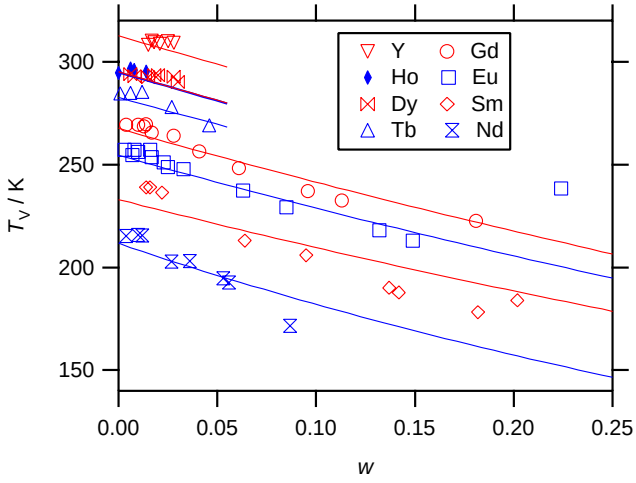

Fig. 9. Experimental T_V values for $R\mathrm{BaFe_2O_{5+w}}$ compared with $T_V(w)$ curves calculated from Eq. (1) and parameters (Table 7) fitted to the $\Delta S(w)$ and $\Delta H(w)$ functions (Fig. 8).

charge ordering. Macroscopically, the action of the added oxygens w is gradual; first the long-range three-dimensional order is destroyed, manifested by disappearance of the superstructure Bragg reflections. Then the remaining sequences of the one-dimensional order along b direction are being removed and disappear at $w \approx 0.25$, and this is manifested by disappearance of the orthorhombic distortion.

Considering the error margins of the DSC method, the fits of the freezing-point-depression model to the main Verwey transition enthalpy and entropy functions of the non-stoichiometry parameter w are good. However, only a qualitative agreement with experimental T_V values is seen in Fig. 9, where the $T_V(w)$ curves derived from the freezing-point-depression model [Eq. (1)] are plotted together with the DSC-based values. The experimental T_V values at $w = 0$ are always higher than those derived from the model, but this is owing to the fact that the experimental data are read from the DSC-peak tops whereas temperatures derived from thermal data refer to the peak centers of gravity. The more significant difference is that the model follows only partially the trend of a steeper decrease in $T_V(w)$ towards $R = \mathrm{Nd}$, and the experimental $T_V(w)$ data are

more concave, even showing a trend to increase close to the situation when the Verwey transition ceases to be discontinuous. No better fit is obtained when the freezing-point-depression model allows $\Delta H(0)$ to change as a function of T according to heat capacities of the solid and melted pure solvent being different, but independent of temperature. First when one considers that the difference of these heat capacities is a linear function of temperature, a better curvature can be obtained. It is however doubtful whether such fitted parameters are real or not. It is interesting to note that neither the model nor the experimental data indicate that $T_V(w)$ is linear. The only thermal parameter that appears to be linear as a function of the non-stoichiometry parameter w is ΔH.

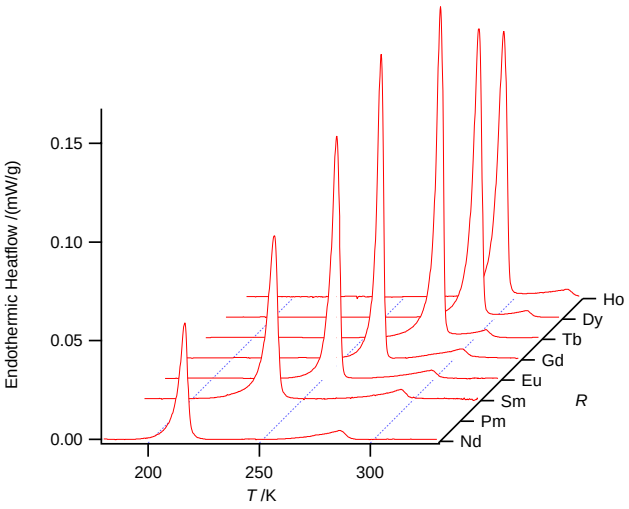

Fig. 10. DSC caloric effects of Verwey transition in RBaFe$_2$O$_5$ upon warming. Selected samples with non-stoichiometry parameter w ranging from $w = -0.001$ (R = Sm) to 0.012 (R = Tb).

3.6. Thermodynamic parameters of Verwey transition in RBaFe$_2$O$_5$

The ideal mixed-valence composition RBaFe$_2$O$_5$ is an important reference point. Fig. 10 illustrates that temperatures and caloric effects of the main charge-ordering Verwey transition in samples approaching such composition vary strongly as a function of R, and obtaining good reference thermal data is essential. Given the error margins in both oxygen-content analyses and thermal values (cf. Fig. 8) such thermal parameters are best obtained from compositional dependences, not from selected individual samples. Moreover, as illustrated in Section 3.1, not all R variants can reach the ideal composition with $w = 0$.

A conservative approach is to fit the thermal data as a function of w with a Gauss curve centered at $w = 0$. This approach has its backing in the probability model of formation of the valence-mixed state suggested in Ref. [12]. Data from such Gaussian fits are available for R = Nd [8], Sm [8], Eu [9], Gd [10], Tb [3], Dy (this work), Ho [5] and Y [4]. Alternatively, thermodynamic parameters for $w = 0$ are extrapolated according to the

Table 8
Thermodynamics[a] of the twin Verwey transitions between the Day–Robin mixed-valence classes in RBaFe$_2$O$_5$

	Class I–II						Class II–III				
R	Peak T_V	ΔH	ΔS	Mean[b] T_V	ΔV[c]	dP/dT_V[d]	Peak T	ΔH	ΔS	Mean[b] T	Refs.
	K	kJ/mol	J/(mol K)	K	J/(mol bar)	bar/K	K	kJ/mol	J/(mol K)	K	
Nd	216.1(3)	1.07(4) *1.14(5)*	5.00(15) *5.38(7)*	214(14)	−0.0235(6)	−211(4)	286.3(13)	0.222(26)	0.79(9)	281(67)	[8]
Sm	238.8(2)	1.68(2) *1.83(14)*	7.26(8) *7.86(16)*	232(6)	−0.0373(10)	−189(2)	295.3(10)	0.168(7)	0.57(2)	294(24)	[8]
Eu	256.3(4)	1.88(4) *1.98(4)*	7.44(13) *7.79(5)*	252(9)	−0.0352(10)	−208(13)	298.8(40)	0.191(7)	0.65(2)	294(23)	[9]
Gd	270.3(10)	2.06(3) *2.16(6)*	7.72(8) *8.08(6)*	267(7)	−0.0336(122)	−226(77)	307.3(15)	0.162(10)	0.54(3)	302(39)	[10]
Tb	285.1(9)	2.45(2) *2.50(8)*	8.69(9) *8.82(8)*	282(5)	−0.0250(8)	−345(8)	308.5(7)	0.173(4)	0.57(2)	305(16)	[3]
Dy	293.5(12)	2.45(3) *2.56(6)*	8.44(10) *8.66(6)*	290(7)	−0.0236(8)	−355(17)	316.4(7)	0.129(8)	0.42(3)	309(38)	Here
Ho	295.7(10)	2.48(7) *2.56(9)*	8.48(27) *8.66(9)*	293(17)	−0.0218(15)	−386(39)	324.5(5)	0.180(15)	0.56(4)	319(51)	[5]
Y	309.5(3)	2.62(3) *2.88(7)*	8.51(9) *9.19(7)*	307(6)	−0.0181(30)	−465(43)	334.2(3)	0.150(8)	0.45(2)	330(35)	[4]

[a] Conservative estimates for ideal RBaFe$_2$O$_5$ ($w = 0$) compositions, obtained from Gaussian-curve fits to the w dependences. Data from the freezing-point-decrease model are in italics.
[b] As given by $\Delta H/T = \Delta S$.
[c] SXPD data for a sample close to $w = 0$, except for R = Gd, which originates from a w dependence.
[d] According to Clapeyron equation, $dP/dT_V = \Delta S/\Delta V$.

model of the freezing-point depression of the charge liquid (Section 3.5). Transition enthalpies and entropies obtained in such manner are larger than those from the first method and can be considered maximum estimates. Parameters of the transitions between the Day–Robin mixed-valence classes I–II and II–III are summarized in Table 8 referring to the standard direction of warming up.

It is seen that enthalpies and transition temperatures of the main transition increase reasonably smoothly across the lanthanoid series as a function of decreasing R^{3+} ionic size (Figs. 11 and 12). Why the 'spectator' R atom exercises such an influence? The likely reason is that lanthanoids are substantially less deformable than Ba. An increasing size of R then becomes less and less compatible with accommodation of the characteristic shape of the doubly occupied d_{xz} orbital of the divalent iron that requires an orthorhombic distortion of the lattice [5]. However, when the ionic size alone is considered, an anomalously high stability of the charge-ordered state is observed for $R = Y$. It can be speculated that a higher atomic polarizability of yttrium is behind this, but the correlation also improves when Allred–Rochow electronegativities [22] are used instead of the ionic radii.

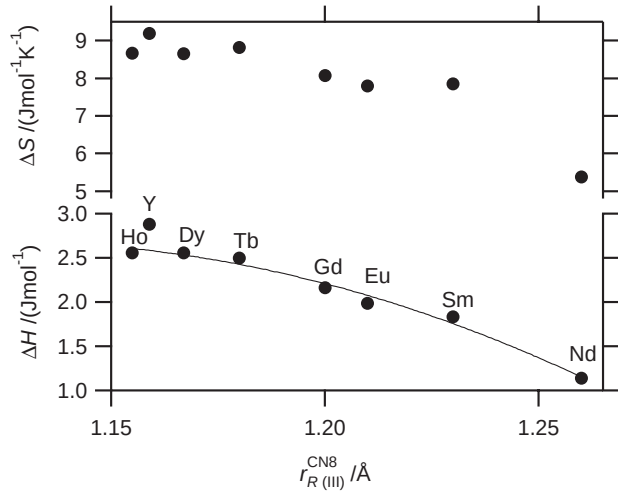

Fig. 11. Enthalpies and entropies of the main Verwey transition in RBaFe$_2$O$_5$, obtained from the freezing-point-depression model, as a function of Shannon [21] 'CR' radii for R^{3+}.

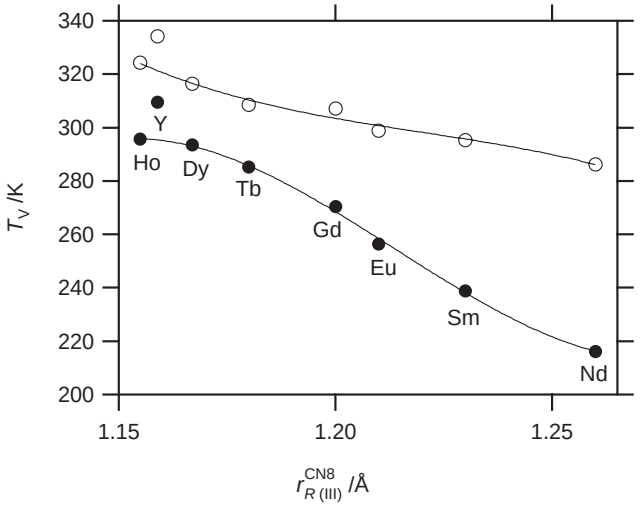

Fig. 12. Premonitory (open symbols) and main (closed symbols) transition temperatures as a function of Shannon [21] 'CR' radii for R^{3+} in RBaFe$_2$O$_5$.

Within the lanthanoid subseries of RBaFe$_2$O$_5$, thermal parameters of the main Verwey transition vary smoothly across the discontinuity in symmetry [5,8] between the long-range charge-ordered variants of $R = Sm$ and Nd. The only parameter that follows this discontinuity is ΔV (Fig. 13 bottom) whereas the slope of the phase boundary $dP/dT_V = \Delta S/\Delta V$ (Fig. 13 top) remains approximately constant. It appears that when the energy balance associated with charge ordering can no longer support the even higher volume increase projected for $R = Nd$, structural deformation occurs for the $R = Nd$ variant allowing it to keep a high level of the $Fe^{2+}d_{xz}$ orbital ordering (Fig. 4).

Why the thermal parameters of the premonitory charge-ordering transition vary so little with R? One reason is that this transition appears to proceed under no volume change. It utilizes the existing small magnetostrictive orthorhombic distortion to perform a similar orbital ordering as the main transition, only in a much smaller extent [3]. It proceeds without any detectable long-range ordering [4], hence between any two iron neighbors along the longer a axis, by increasing the bond-valence sum for one of them at the expense of the other. Since the strength of the magnetic interactions can be measured in terms of the Néel temperature T_N, and T_N is constant across the R series [5], the temperature of the premonitory charge-ordering

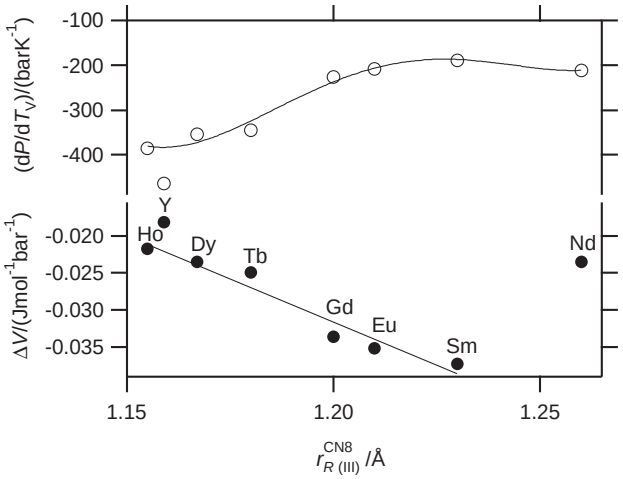

Fig. 13. Volume parameters of Verwey transition in RBaFe$_2$O$_5$ as a function of Shannon [21] 'CR' radii for R^{3+}.

transition varies less as a function of R than does the main transition temperature T_V.

4. Conclusion

Key aspects of the twin charge-ordering transitions in RBaFe$_2$O$_5$ can be understood by considering conditions for ordering of the (nearly) degenerated doubly occupied d_{xz} orbitals of divalent iron as the primary cause of disproportionation of the thermally induced valence-mixed $Fe^{2.5+}$ states. The effect of other structural and compositional variables depends on their compatibility with the symmetry of the spatial electrostatic interactions defined by the shape of the d_{xz} charge as opposed to a point-charge model. The 'spectator' ions with approximately spherical symmetry influence the charge ordering via their variable size and deformability. Magnetic interactions appear to have their say, via the magnetostrictive effect, which is essential in defining the direction of the symmetry breakings under the subsequent charge-ordering transitions.

Based on series of observations on this structurally very simple RBaFe$_2$O$_5$ model, a definition of the Verwey-type transition can be offered: Upon cooling, it occurs in an extended crystalline solid as a disproportionation of a thermally induced valence-mixed state into two states of which *one* has one doubly occupied, or a sole singly occupied, t_{2g} orbital in bond network of symmetry that allows these orbitals to order mutually. These attributes comply with the original Verwey observations that the transition is a first-order charge ordering accompanied by a pronounced change in electrical conductivity owing to the electron localization. Examples include the well-known mixed-valence high-spin Fe^{2+}, Fe^{3+} combinations in ligand fields related to distorted octahedra and the V^{4+}, V^{5+} couples. A conjecture based on this definition would be that glasses and fully disordered systems with such Fe^{2+}, Fe^{3+} ions will not experience Verwey transition as discontinuous, unless ordering of the doubly occupied d_{xz} orbitals of divalent iron can be accommodated within the type of the disorder. Finally, predictions of new Verwey-type systems in distorted octahedral fields would include low-spin d^4, d^3 combinations such as Ru^{4+}, Ru^{5+} and Re^{3+}, Re^{4+} couples.

When *both* prospective charge-ordered ions possess dominant valence-electron shapes that allow their mutual ordering, thermal energy may not be sufficient to stabilize the valence-mixed ground state, and only the charge-ordered phase is known. This appears to be the case of YBaMn$_2$O$_5$. On the other hand, if there are two doubly or two sole singly occupied nearly degenerated orbitals, these may also order, but their thermally induced mixing would proceed gradually and the transition would not be of the first order. That is the case of YBaCo$_2$O$_5$.

Acknowledgments

Experimental assistance from the staff of the Swiss-Norwegian Beam Lines at ESRF is gratefully acknowledged.

Supporting information: CIF files can be obtained from the Fachinformationszentrum Karlsruhe, 76344 Eggenstein-Leopoldshafen, Germany, (fax: (49)7247-808-666; e-mail: crysdata@fiz-karlsruhe.de) on quoting the depository number CSD 413169 for charge-ordered DyBaFe$_2$O$_5$ at 200 K and CSD 413170 for valence-mixed DyBaFe$_2$O$_5$ at 330 K.

References

[1] M.B. Robin, P. Day, Adv. Inorg. Chem. Radiochem. 10 (1967) 247.
[2] N.F. Mott, Philos. Mag. B 42 (1980) 327.
[3] P. Karen, P.M. Woodward, J. Lindén, T. Vogt, A. Studer, P. Fisher, Phys. Rev. B 64 (2001) 214405.
[4] P.M. Woodward, P. Karen, Inorg. Chem. 42 (2003) 1121.
[5] P.M. Woodward, E. Suard, P. Karen, J. Am. Chem. Soc. 125 (2003) 8889.
[6] E.J.W. Verwey, Nature (London) 144 (1939) 327.
[7] P.W. Anderson, Phys. Rev. 102 (1956) 1008.
[8] P. Karen, P.M. Woodward, P.N. Santhosh, P.W. Stephens, S. Pagola, J. Solid State Chem. 167 (2002) 480.
[9] P. Karen, Unpublished.
[10] P. Karen, J. Solid State Chem. 170 (2003) 9.
[11] M. Sorai, D.N. Hendrickson, Pure Appl. Chem. 63 (1991) 1503.
[12] J. Lindén, P. Karen, A. Kjekshus, J. Miettinen, T. Pietari, M. Karppinen, Phys. Rev. B 60 (1999) 15 251.
[13] J. Nakamura, J. Lindén, H. Yamauchi, M. Karppinen, Solid State Commun. 121 (2002) 269.
[14] P. Karen, P.M. Woodward, J. Mater. Chem. 9 (1999) 789.
[15] A.C. Larson, R.B. Von Dreele, General Structure Analysis System (GSAS), Los Alamos National Laboratory Report LAUR 86-748 (version 1998 used).
[16] P.W. Stephens, J. Appl. Crystallogr. 32 (1999) 281.
[17] P. Thompson, D.E. Cox, J.B. Hastings, J. Appl. Crystallogr. 20 (1987) 79.
[18] P. Karen, O. Braaten, H. Fjellvåg, A. Kjekshus, in: AMSAHTS '90, Goddard Space Flight Center, Greenbelt, MD, April 2–6, 1990, NASA Conf. Publ. Vol. 3100, 1991, p. 117.
[19] W. Zhang, K. Osamura, Mater. Trans. JIM 32 (1991) 1048.
[20] I.D. Brown, Accumulated table of bond valence parameters, version 1999.03.26, personal communication.
[21] R.D. Shannon, Acta Crystallogr. Ser. A 32 (1976) 751.
[22] A.R. Allred, G.E. Rochow, J. Inorg. Nucl. Chem. 5 (1958) 246.